Optimizing the Performance of a Solar Air Collector's Flat Plate Absorbed at Different Locations through Combined Thermal and Optical Modeling

Hiwa Abdlla Maarof

Mechanical engineer

hiwa.maarof@uoh.edu.iq

abstract

Increasing the absorber plate surface in a solar air heater system (SAHs) can increase thermal efficiency. This paper includes the development of a 3-dimensional computational fluid dynamics (3-D CFD) model for predicting the location of the absorber plate from the bottom of the collector, followed by its validation using experimental data. Various geometrical types are investigated to determine optimal design features, such as Type I with no distance from the collector's bottom, Type II, Type III, Type IV, and Type V with a distance (dis) of 0.002, 0.004, 0.006, and 0.008m. A comprehensive analysis is performed to achieve this goal, including thermal efficiency, heat transfer coefficient, and Nusselt number analyses. Results indicate that Type V has better performance than other geometries. so that the absorber plate location with dis of 0.008 m, the maximum daily thermal efficiency, heat transfer coefficient, and Nusselt number of the system was obtained at 84.75%, 17 (W/m^2. K), and 21.1. while the thermal efficiency, heat transfer coefficient, and Nusselt number of the system were less than 76.6%, 9.7 (W/m^2. K), and 6.75 when the absorber plate was lying on the collectors without a gap between absorber and collector bottom. Compared with conventional systems under the same conditions, the current system is more efficient in terms of thermal efficiency, heat transfer coefficient, and Nusselt number.

Keywords: Solar Air Heater; 3-D CFD Modeling; Optical and Thermal Modeling; Heat Transfer Coefficient; Nusselt Number; Thermal Efficiency

١. Introduction

Worldwide economic progress and industrialization have become increasingly dependent on energy in various forms. Climate change and sustainable development make solar energy an essential energy source. There is no limit to the amount of energy that can be derived from solar radiation, making it a central and infinite resource. A solar air heater is the simplest way to convert solar energy into thermal energy. Because of their simplicity and low cost, solar air heaters are one of the most commonly used types of solar thermal systems [1]. Solar radiation, both direct and diffuse, is absorbed in the absorber plate, which transfers this energy to the air flow rate through the absorber plate. The beneficial heat gain by the collector fluid determines the thermal efficiency of solar air heaters [2]. Sunlight and heat are both forms of solar energy. A significant advantage of this renewable energy is that it is one of the most significant and promising energy sources. It is estimated that the sun's energy that falls on the surface of the Earth is about ten thousand times its current energy requirement [3].

Solar air heaters (SAHs) are heat exchangers used in low-temperature processes. The absorber plate transforms solar radiation into heat at the SAHs. Due to the thermophysical properties of air, the main disadvantage of SAHs is the low thermal efficiency [4]. Using obstacles, baffles, expanded, finned, or corrugated surfaces as absorbing surfaces can significantly improve the energy efficiency of SAH [5–9]. In recent years, there has been an essential change in this situation. This is because global efforts have improved access to and ensured energy security and mitigating climate change [10–12]. There are a variety of applications for solar energy, including solar drying [13–16]. solar thermal power [17–19]. concentrated solar power [20,21]. solar ponds [22,23]. solar space heating and cooling [24–26]. solar furnaces [27]. and solar water heating [24,28].

Nomenclature

Variables		Subscripts	
A_c	Collector area(m^2)	a	Air
c	Vacuum speed (m/s)	ab	Absorber
C_p	specific heat at constant pressure (kJ/kg K)	amb	Ambient
D	Diameter(m)	b	Boundary
D_h	Hydraulic diameter(m)	Col	Collector
g	Gravitational acceleration(m/s^2)	g	Glass
h	heat transfer coefficient, (W/m^2 K)	In	Inlet
I	Irradiation intensity (W/m^2)	Op	Optical
I_g	Global solar irradiation(W/m^2)	Out	Outlet
$\dot{m}$	Mass flow rate(kg/s)	P	Plate
n	Refraction index	rad	Radiation
n_i	Incidence ray unit vector	S	Surface
n_r	Reflected ray unit vector	th	Thermal
n_s	Surface normal vector	w	Wind
P	Pressure (Pa)	Greek Symbols	
P_k	Production term	α	Absorptivity
q	Initial ray position vector(m)	ε	The emissivity of the absorber plate
q	Heat flux (W/m^2)		
q_c	solar radiation on the collector (W/m^2)	η	Efficiency
Q_b	Boundary heat source(W)	μ	Dynamic viscosity ($kg/m.s$)
Q_u	Useful heat gain(W)		
q_c	solar radiation on the collector (W/m^2)		
$\dot{Q}_T$	total solar energy (kW)		
r	Ray position vector(m)	Greek Symbols	
T	Temperature (°C)	α	Absorptivity
t	Time (h)	k	Thermal conductivity(W/m.k)
u	Velocity (m/s)	k	Wave vector
U_w	Ambient wind velocity(m/s)	θ_i	Incident angle(rad)
W	Duct width	θ_t	Refractive angle(rad)
	Abbreviation	σ	Stefan-Boltzmann constant
CFD	Computational fluid dynamics	τ	Transmittivity
$FSAH$	Flat solar air heater	w	Angular frequency
GOP	Geometric optics	k	Thermal conductivity(W/m.k)
$RSAH$	Solar air collector with roughness surface	k	Wave vector
SAH	Solar air heater	θ_i	Incident angle(rad)

The use of different types of SAHs has been reported in several studies. Kumar *et al*. [29]experimentally investigated the thermal energy and outlet temperatures. The experimental results were increased from 17 % to 46 % when compared with the smooth channel. Aboghrara *et al*. [30] tested flat plate absorbers compared with corrugated absorber plates. Showed the effect of jet impingement through circular jets in a duct flow of solar air heaters. They found that a substantial heat transfer enhancement effect has inflow jet impingement on corrugated plating absorbers. It is observed that the proposed design duct has almost 14% higher thermal efficiency than the smooth duct. Luan *et al*. [31] experimentally analyze for baffles angle from 60° to 120° that caused the most significant turbulence due to increasing degree of blockage and obtained high efficiency. Singh *et al*. [32] experimentally evaluated flat plate and flat plate with small cylindrical tubes with and without phase change material (PCM), indicating that Compared to SAH with a flat plate absorber on forced convection, SAH with PCM-filled small cylindrical tubes has a temperature difference between ambient air and exhaust air of about 2℃ to 9℃. Provided outlet temperatures at about 48 ◦C for approximately 9.8 hours/day at least, with 66% daily efficiency. Azad *et al*. [33] Performed a comprehensive experimental comparison between the rib elements diameter (g/e) of 2, 3, 4, and 5 at an airflow angle 30◦, at Reynolds numbers 3000 to 14000. Nusselt number is maximally enhanced at g/e equal to 4, which is 3.88 times greater than smooth plates. Saravanan *et al*. [34] experimental investigation of the SAHs utilized multiple staggered C-shaped finned absorbers, both perforated and unperforated, 3.3 to 3.8 ratio of pitch to the gap, 0.3 to 0.7 ratio of height, and 1.5 to 3 ratio of perforations, in order to maximize heat transfer. The highest thermal performance was achieved at the relative pitch to gap ratio of 3.8, the relative height ratio of 0.6, and the corresponding perforation ratio of 3. For 3.8 and 0.6 relative pitch to gap ratios and 0.6 relative height ratios, respectively, thermal performance and friction factor of C-shaped finned absorber plates without perforated holes were 2.61 and 5.93 times higher than flat absorber plates. khanlari *et al*. [35] experimental and numerical analyses for a tube-type SAH drying process were conducted, and the results indicate that it can achieve an efficiency of 45.6-56.8%. Abo-Elfadl *et al*. [36] compared single-pass Flat_SAH and single-pass T_SAH at 0.025 kg/s and found increased thermal and exergy efficiencies in single-pass T_SAH compared to single-pass F_SAH, attained thermal and exergy efficiencies of 133% and 330%, respectively. Singh *et al*. [37] Systematically surveyed the thermal performance of a porous serpentine wavy wire mesh packed bed solar air heater. In a

93% porous double pass serpentine packed bed SAH, the thermal and thermohydraulic efficiencies were approximately 80% and 74%, respectively. That is 18% and 17% higher than a single pass. Bensaci *et al*. [38] tested numerical and experimental studies on four cases depending on the baffle placement with Reynolds numbers from 2370 to 8340. An analysis of the effects of baffle positions on convective heat transfer coefficients has been conducted. Solar air heaters achieve the best thermo-hydraulic efficiency if the baffles are located in the first 50% of the air channel. Farhan *et al*. [39] In an experimental and numerical study of energy efficiency and exergetic efficiency of v-corrugated SAHs, twisted tape inserts are placed within the air passages formed by the absorber and backplate. Thermal and thermohydraulic efficiencies can be increased by 17.5 and 17%, respectively, compared to absorbers without twisted tape.

An analysis of solar heaters' shortcomings in the presence of an air absorber plate is presented and a proper strategy is proposed to improve their efficiency. Based on the experimental results from a flat plate in SAHs, a 3D CFD model is developed. This model uses the Optics Geometric component in combination with the heat transfer in solid and fluid components to evaluate the daily performance of different absorbing surfaces and absorber plate locations using the instantaneous actual flux distributions. The radiative and heat losses are taken into account. Validation of the model is based on experimental evidence produced from a system with the same components and dimensions under various operating conditions. After simulation validation, the model is modified for various absorber plate locations. the system thermal efficiency analysis is carried out. Finally, the efficiency of the air heater from the viewpoints of outlet temperatures, thermal efficiency, heat transfer coefficient, and Nusselt number are evaluated. This is done using COMSOL Multiphysics 5.6 which can simulate and do these problems well.

٢. Experimental Conditions

A clean daytime environment was used for testing Esen [40]. Firat University, Faculty of Technical Education, Turkey, installed and measured a SAH in Elazig (latitude 38.41 N, altitude 1067 m above sea level, longitude 39.14 E). SAHs can be modeled using a WNN-based optimization method. Based on predictions and experimental results, estimate the efficiency of SAHs more accurately with the proposed WNN model. SAHs with an absorbing surface and

their airflow rates. A schematic and a diagram of the flat plate absorber are shown in **Fig. 1**. The absorber plate was used in this application. The stainless-steel absorber was coated with black chrome. This absorber has a dimension of 0.84, 2.14 m, and a thickness of 1 mm. Glass was 5 mm thick. The collector used a single cover glass, after installation, the collector ran for many days under normal weather conditions. On the surface of the absorber plate were evenly spaced thermocouples, measured the collector's inlet and outlet temperatures using two thermocouples with well-insulated leads. The environment temperature was measured with a mercury thermometer behind the collector. To determine whether Collectors are exposed to a total amount of solar radiation, a Kipp and Zonen CM 11 Pyranometer was used. The meter is adjacent to the glazing cover and on the same plane. Solar radiation was measured automatically by a Kipp and Zonen CC 12 solar integrator. An airflow meter (Lutron AM-4206M digital anemometer) was used to collect data at 30-minute intervals on insolation, working fluid outlet and inlet temperatures, ambient temperature, and absorbing plate temperature. Radial fans provided the air with a maximum power of 0.537 kW each. The collector's outlet was fitted with an air-sucking radial fan. Inlet and outlet pressure losses were measured with a digital manometer (AZ 82100). This study simultaneously measured the ambient temperature, collector temperatures, air velocity, pressure, and solar radiation as the air passed through the duct and moved through the collectors. A digital manometer (AZ 82100) has a 3% accuracy, and a Kipp and Zonen CM11 Pyranometer has a 1% accuracy. At the same time, the experiment was conducted using T-type thermocouples, which are accurate to 0.018 degrees Celsius, metal-vane anemometers (AM-4206M, air velocity + airflow), and Kipp and Zonen CM11 Pyranometers. A series of tests were administered between 9:00 to 16:00.

a

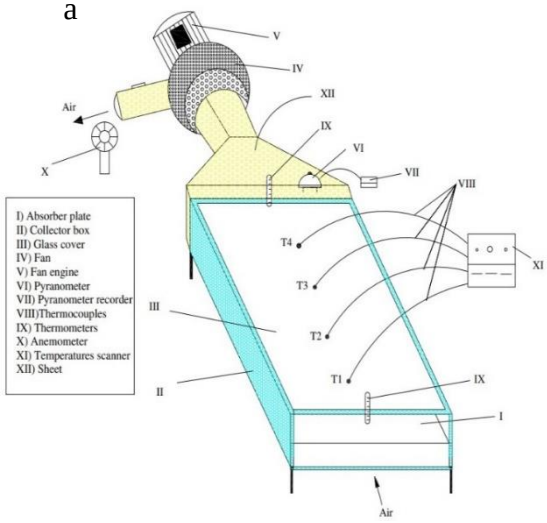

b

Fig. 1 (a), Diagram of the SAHs, (b), flat plate absorber of the experimental

۳. Explanation Analytical

۳،۱. Optical Modeling

The Geometric Optics (GOP) module of the COMSOL Multiphysics software 5.6 is used to simulate ray trajectory in the SAHs and gather realistic solar flux distributions on the absorber's surface and position from the base of the collector. This model calculates distributed fluxes and solar thermal energy absorbed by surfaces based on the optical properties of the glass cover and absorb plate. This ray tracing model reflects the original optical properties of all components. Glass is modeled to have a transmission coefficient of 0.9, an emissivity of 0.5, and an absorption coefficient of 0.9 for the absorbing coating. Components of the design are shown in **Fig. 2**.

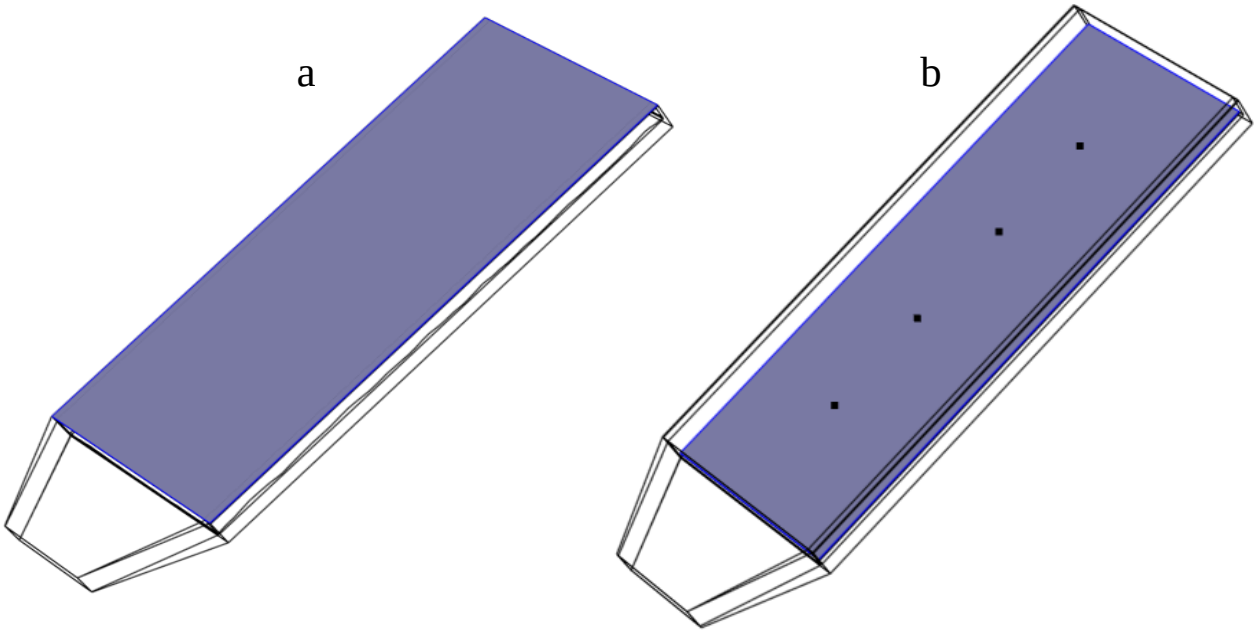

Fig. 2 an optical system consists of (a) glass cover, (b) absorber plate

In Wavefront Ray Tracing, the ray directions and incidence angles are determined using the Fresnel equation and Snell's law. Each ray's propagation can be described by first-order equations coupled together.

$$\frac{dq}{dt} = \frac{\partial w}{\partial k} \qquad (١)$$

q represents the position vector

$$\frac{dk}{dt} = -\frac{\partial w}{\partial q} \qquad (٢)$$

k represents the wave vector

$$\theta_i = a\cos\left(\frac{n_i . n_s}{|n_i||n_s|}\right) \qquad (٣)$$

(*ni*) is a normal vector in the domain of air that (θi) and (*ns*) represent the normal angle of incidence and a unit vector for incident rays. Reflected rays travel in the same direction as (*nr*):

$$n_r = n_i - 2n_s \cos\theta_i \qquad (٤)$$

n_t represents the propagation direction of the refracted ray

Angular frequency and ray vector are related by the following expression:

$$w = \frac{c}{n} \qquad (٥)$$

The model shows that the glass cover is transparent, allowing solar radiation to pass through it. A very slight diffuse and specular reflection is visible from the surface, as shown in **Fig. 2** a. Next is the black absorber plate, which is more thermally conducting, as shown in **Fig. 2** b.

٣,٢. Optical-thermal model combined

To understand the related phenomena within a system, it is critical to examine the impacts of the essential parameters on its performance. Developing an accurate and helpful model requires being comprehensive and straightforward and able to describe and predict behavior under conditions similar to the real world. An optical system model is proposed, then a thermal and fluid flow model is constructed using the heat flux distribution from the optical model. To determine whether solar flux distributions on absorbing plates are not uniform, we used the geometric optics module in COMSOL Multiphysics 5.6.

Table 1 Thermal and Optic Geometric Properties of Solar Air Heaters.

Parameters and components	**Specifications, properties, and values**
Sun rays' number	100,000
Index of refraction of exterior domains	1
Maximum secondary ray number	0
SAH(Glass)	Solar transmittance of glass: 0.9
	Glass solar absorption: 0.02
	The refraction index of glass: 1.45
	The emissivity of the glass: 0.5
Irradiance and power	maximum irradiance: 970 W/m^2
	Average irradiance: 809 W/m^2

	Max. power: 1797 W.
SAH	Solar air collector thickness: ٠,٠٣ m
	Solar air collector length: ٢,١٤ m
	Solar air collector width: ٠,٨٤ m
	Collector angle: (٣٠ °).
Glass	Glass thickness: ٠,٠٠٥ m
	Glass density: ٢٢٠٣ kg/m^{٣}
SAH (absorber)	Heat transfer fluid: Air
	Absorber material: copper
	Collector area: ١,٨ m^{٢}
	Absorber thickness: ٠,٠٠١ m
	Coating emissivity: ٠,٩٤
	Absorber thermal conductivity: ٤٠٠ W/(m.K)
Operational Parameters	Inlet mass flowrate: ٠,٠٢-٠,٠٦ kg/s.
	Inlet temperature: ٢٤-٣٨,٦ °C
	Wind velocity: ١ m/s
	Ambient temperature: ٢٤-٣٨,٦ °C

٣,٣. Energy and Fluid Flow Modeling

As ambient and time variations in solar radiation affect incoming solar radiation, it is evaluated as the system is operated to estimate its energy balance under unsteady-state conditions. As a result of energy balance across the entire system, the following equation can be expressed:

$$\frac{\partial\left(\rho C_p T\right)}{\partial t} + \rho C_p u.\nabla T + \nabla.\left(-k\nabla T\right) = 0 \qquad (٦)$$

Thermal capacity is expressed by C_p, density by ρ, and thermal conductivity by k in this formula. Additionally, u represents the airflow velocity field through the box.

In the Geometric Optics module, thermal analysis was applied to determine how much heat should be absorbed on the collector walls by a solar heat plate. In order to calculate the energy formula, embedded solar heat must be taken into account. The heat flux of a system also includes thermal losses analysis. Using Newton's cooling law, convective heat is calculated by measuring the amount of heat transferred from the surface of the glass to the surrounding air.

$$Q_{loss,conv} = h_{conv} A_{glass} \left[T_{glass}(t) - T_{amb}(t) \right] \quad (٧)$$

An air surface and a glass surface are coupled by convection induced by h_{conv}. A flat plate absorber's radiative heat loss is based on using the Stefan-Boltzmann radiation exchanging equation:

$$Q_{loss,rad}(t) = \varepsilon \sigma A_{abs} \left[T_{s,abs}^4(t) - T_{amb}^4(t) \right] \quad (٨)$$

The ε parameter measures how much light the absorber absorbs and provides this Stefan-Boltzmann constant. Collectors have thermally insulated sides and bottoms.

In this study, the inlet air mass flow rate ranges between 0.02 and 0.08 kg/s. Thus, the Reynolds number of the air should be used to select the fluid flow model module. The purpose is to determine the velocity field inside the SAHs. The equation is as follows:

$$\frac{\partial \rho}{\partial t} + \nabla.(\rho u) = 0 \quad (٩)$$

The momentum formula describes how air moves in the collector:

$$\rho \frac{\partial u}{\partial t} + \rho (u.\nabla) u = \nabla.\left[-pI + (\mu + \mu_T)(\nabla u + (\nabla u)^T) \right] + \rho g \quad (10)$$

Time-dependent governing equations determine the thermal efficiency of the SAHs.

$$\eta_{th}(t) = \frac{\dot{m} c_p \left[T_{Out}(t) - T_{In}(t) \right]}{I_g(t) A_c} \quad (١١)$$

Nu is determined as follows:

$$Nu = \frac{h \times D_h}{K} \quad (١٢)$$

h the heat transfer coefficient in the SAHs determined as follows:

$$h = 2.8 + 3U_{wind} \quad (13)$$

D_h is a hydraulic diameter calculated as follows:

$$D_h = \frac{A_{cross}}{P_{wet}} \times \frac{L_c}{L_c} = \frac{4V_{air}}{A_{contact}} \quad (١٤)$$

٣,٤. Defining the boundary and the initial conditions

These boundary conditions govern collector air flow rates and heat transfer:

$$-\int \rho(u.n)ds\,|_{in} = \dot{m} \quad (١٥)$$

$$T_{in}(t) = T_{amb}(t) \quad (١٦)$$

A heat absorber plate displays the amount of heat absorbed as follows:

$$-n.k\nabla T\,|_{boundary} = Q_b \quad (١٧)$$

When solving time-dependent governing equations, the absolute ambient temperature at the time the system was started is assumed.

$$T_{In} = T_{amb} \quad (١٨)$$

٤. Model Validation and Mesh Independence Analysis

٤,١. Grid validation independently

The mesh elements in the CFD modeling were created using a free tetrahedral grid in COMSOL Multiphysics 5.6. When a mesh control custom mesh generation defines this

parameter, highly dense meshes are generated for the absorber plate, solar air heater, and air within the collector. Provides qualitative insight into how the mesh was shaped for modeling the system shown in **Fig. 3**. Having a margin of error below 3% is used to estimate the input solar energy due to developing independence criteria for meshes, and air running through the collector absorbs the sum of heat. **Table 2.** provides information on the number of grids. With the increase in the number of cells, outlet temperatures remained unchanged due to the mesh study. It is evident from **Table 2**. that a total of 803819 cells were independent.

Table ٢. Mesh Independence Analysis

Time(h)	Mesh Elements Specifications			Exp. Temperature(°C)	Model. Temperature (°C)	Relative Error (%)
	Domain	boundary	edge			
	٣٨٤٦٧٥	٧٧٢٣٤	٢٤٠٤	٤٢,٥	٤٣,٤	٣,٥٦
١١:٠٠	٦٩١٩٥٢	١٤٨٥٢٤	٣٥٣٤	٤٢,٥	٤٣,١	٣,٦٧
	٨٠٣٨١٩	١٧٢٨٧١	٣٧٦٧	٤٢,٥	٤٢,٩	٣,٧
	٨٤٤٧٠٣	١٧٩٠٥٩	٤١٢٧	٤٢,٥	٤٣,١٢	٣,٦٥
	٣٨٤٦٧٥	٧٧٢٣٤	٢٤٠٤	٤١	٤٣,٧٥	٢,٨٣
١٣:٠٠	٦٩١٩٥٢	١٤٨٥٢٤	٣٥٣٤	٤١	٤٣,٢٣	٢,٩٩
	٨٠٣٨١٩	١٧٢٨٧١	٣٧٦٧	٤١	٤٢,٨٩	٣
	٨٤٤٧٠٣	١٧٩٠٥٩	٤١٢٧	٤١	٤٣,٥٣	٢,٩
	٣٨٤٦٧٥	٧٧٢٣٤	٢٤٠٤	٣٨	٤٠,٥٧	١,٨٥
١٤:٠٠	٦٩١٩٥٢	١٤٨٥٢٤	٣٥٣٤	٣٨	٤٠,١٢	١,٩٩
	٨٠٣٨١٩	١٧٢٨٧١	٣٧٦٧	٣٨	٣٩,٩٣	٢
	٨٤٤٧٠٣	١٧٩٠٥٩	٤١٢٧	٣٨	٤٠,٣١	١,٩٣
١٥:٠٠	٣٨٤٦٧٥	٧٧٢٣٤	٢٤٠٤	٣٢	٣٦	٠,٤٤
	٦٩١٩٥٢	١٤٨٥٢٤	٣٥٣٤	٣٢	٣٥,٦٢	٠,٥٧
	٨٠٣٨١٩	١٧٢٨٧١	٣٧٦٧	٣٢	٣٥,٤٤	٠,٦٣
	٨٤٤٧٠٣	١٧٩٠٥٩	٤١٢٧	٣٢	٣٥,٧٣	٠,٥٤

٤,٢. Model verification

As part of this validation, experimental results were compared to the model's predictions to ensure that the proposed model is accurate. Various operating conditions are compared in **Table**

3. The average air temperature in the system is estimated by comparing models with experimental data (T1, T2, T3, T4, and T_outlet). In order to validate a model, (T1, T2, T3, T4, and T_outlet) must be measured relative to each other. Eqs can be used to express these errors.

$$E_T = \left| \frac{T_{Out,num} - T_{Out,Exp}}{T_{Out,Exp}} \right| \times 100 \qquad (١٩)$$

Despite various operating conditions, model results and experimental data show good agreement in **Table 3**. It is also parametrically suitable, in addition to being reliable. Therefore, the system's heat losses can be considered when evaluating the model.

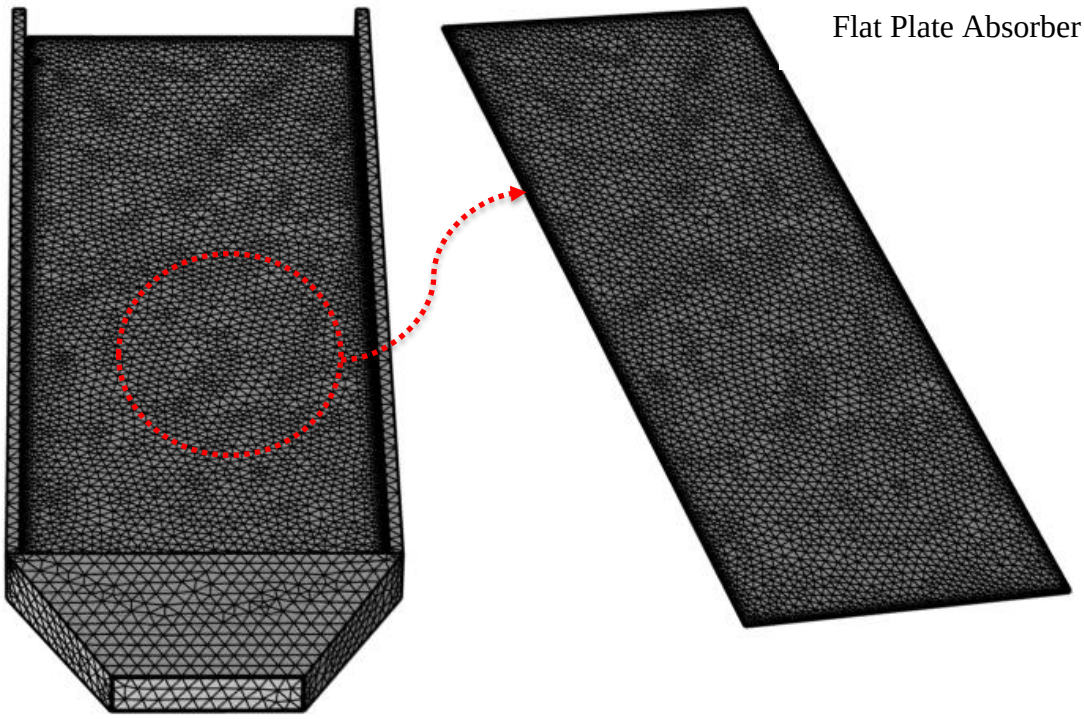

Fig. ٣ The meshes generated for the CFD simulation of solar collectors

Table ٣. Validation Experimental Temperatures

Ta_in (˚C)	Model .T١ (˚C)	Exp.T ١ (˚C)	R_Erro r (%)	Model. T٢ (˚C)	Exp.T ٢ (˚C)	R_Erro r (%)	Model.T ٣ (˚C)	Exp.T ٣ (˚C)	R_Erro r (%)	Model. T٤ (˚C)	Exp. T٤ (˚C)	R_Erro r (%)	Model.T_ out (˚C)	Exp.T_ out (˚C)	R_Erro r (%)
٢٣,١	٢٥,٠	٢٥,٣	٠,١٠	٢٥,٠٠	٢٦,٢	٠,٤٠	٢٥,٠٠	٢٧,١	٠,٧٠	٢٥,٠٠	٢٧,٧	٠,٩٠	٢٥,٠٠	٢٩,٠	١,٣٢
٢٧,١	٣٤,٢	٣٥,٤	٠,٣٩	٣٦,١٣	٣٨,٢	٠,٦٧	٣٩,٢٨	٣٩,٨	٠,١٧	٤١,١٩	٤١,١	٠,٠٣	٤٣,١٨	٤١,٩	٠,٤١
٣١,٢	٣٩,٤	٣٩,٥	٠,٠٤	٤٢,٠٣	٤٤,٠	٠,٦٢	٤٦,٤١	٤٦,٥	٠,٠٣	٤٩,١٢	٤٨,٠	٠,٣٥	٥٢,٣٠	٤٩,٩	٠,٧٤
٣٣,٨	٤٢,٨	٤٢,٥	٠,١٠	٤٥,٩٣	٤٧,٢	٠,٤٠	٥١,٠٧	٥٣,٠	٠,٥٩	٥٤,٣٠	٥٥,١	٠,٢٤	٥٨,٢٠	٥٦,٩	٠,٣٩
٣٥	٤٤,٤	٤٥,٩	٠,٤٧	٤٧,٧٤	٤٩,٥	٠,٥٥	٥٣,٢١	٥٦,٦	١,٠٣	٥٦,٦٧	٥٩,٢	٠,٧٦	٦٠,٩٧	٦٢,٩	٠,٥٧
٣٦,٦	٤١,٧	٤١,٠	٠,٢٣	٤٤,٩٥	٤٥,٠	٠,٠١	٥٠,٢٥	٤٩,٩	٠,١١	٥٣,٦٢	٥٣,٠	٠,١٩	٥٨,٠١	٥٦,٨	٠,٣٧
٣٧,٩	٣٧,٩	٣٨,٠	٠,٠٢	٤٠,٧٣	٤٢,٠	٠,٤٠	٤٥,٣٣	٤٤,٠	٠,٤٢	٤٨,٢٨	٤٦,٥	٠,٥٦	٥٢,٢٩	٤٩,٠	١,٠٢
٣٩,٢	٣٣,٢	٣٢,٠	٠,٣٩	٣٥,٤٠	٣٤,٨	٠,١٩	٣٩,٠٤	٣٦,٠	٠,٩٨	٤١,٤٠	٣٧,٤	١,٢٩	٤٤,٧١	٣٩,٠	١,٨٣
٣٩,٩	٢٥,٠	٢٥,٣	٠,١٠	٢٥,٠٠	٢٦,٢	٠,٤٠	٢٥,٠٠	٢٧,١	٠,٧٠	٢٥,٠٠	٢٧,٧	٠,٩٠	٢٥,٠٠	٢٩,٠	١,٣٢
٣٨,٦	٣٤,٢	٣٥,٤	٠,٣٩	٣٦,١٣	٣٨,٢	٠,٦٧	٣٩,٢٨	٣٩,٨	٠,١٧	٤١,١٩	٤١,١	٠,٠٣	٤٣,١٨	٤١,٩	٠,٤١
٣٧	٣٩,٤	٣٩,٥	٠,٠٤	٤٢,٠٣	٤٤,٠	٠,٦٢	٤٦,٤١	٤٦,٥	٠,٠٣	٤٩,١٢	٤٨,٠	٠,٣٥	٥٢,٣٠	٤٩,٩	٠,٧٤
٣٥,٦	٤٢,٨	٤٢,٥	٠,١٠	٤٥,٩٣	٤٧,٢	٠,٤٠	٥١,٠٧	٥٣,٠	٠,٥٩	٥٤,٣٠	٥٥,١	٠,٢٤	٥٨,٢٠	٥٦,٩	٠,٣٩
٣٤	٤٤,٤	٤٥,٩	٠,٤٧	٤٧,٧٤	٤٩,٥	٠,٥٥	٥٣,٢١	٥٦,٦	١,٠٣	٥٦,٦٧	٥٩,٢	٠,٧٦	٦٠,٩٧	٦٢,٩	٠,٥٧
٣٣,٤	٤١,٧	٤١,٠	٠,٢٣	٤٤,٩٥	٤٥,٠	٠,٠١	٥٠,٢٥	٤٩,٩	٠,١١	٥٣,٦٢	٥٣,٠	٠,١٩	٥٨,٠١	٥٦,٨	٠,٣٧
٢٩,٨	٣٧,٩٥	٣٨,٠	٠,٠٢	٤٠,٧٣	٤٢,٠	٠,٤٠	٤٥,٣٣	٤٤,٠	٠,٤٢	٤٨,٢٨	٤٦,٥	٠,٥٦	٥٢,٢٩	٤٩,٠	١,٠٢
Relative Error %			٠,٢٢			٠,٤١			٠,٥٠			٠,٥٤			٠,٨٣

٥. The Results and Discussion

٥,١. Solar Fluxes and Ray Trajectory Distributions

Solar air collectors are predicted to have ray trajectories and flux distributions. The collector surface interferes with reflections on the absorbing surface and concentrates them in irregular patterns. In order to show how rays, cross a collector, a ray is focused on an absorbing surface shown in **Fig. 5** a, A surface with a distributed solar flux. A collector surface's solar flux distribution is also shown in **Fig. 5** b.

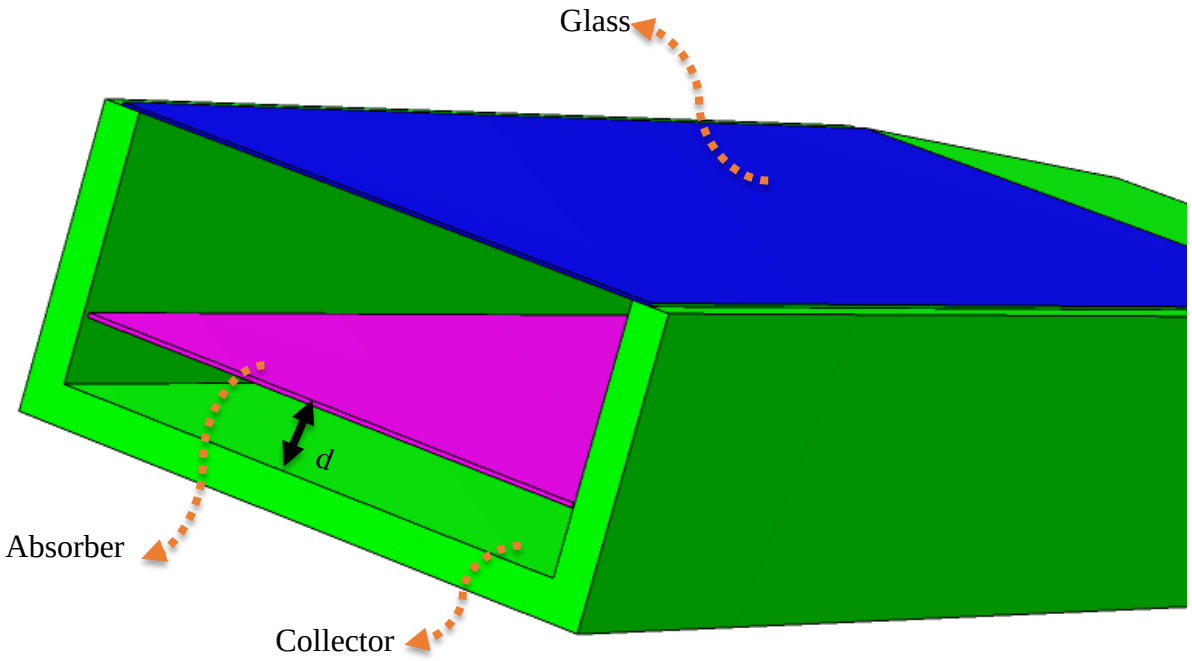

Fig. ٤ The location of the absorber plate relative to the collector bottom line.

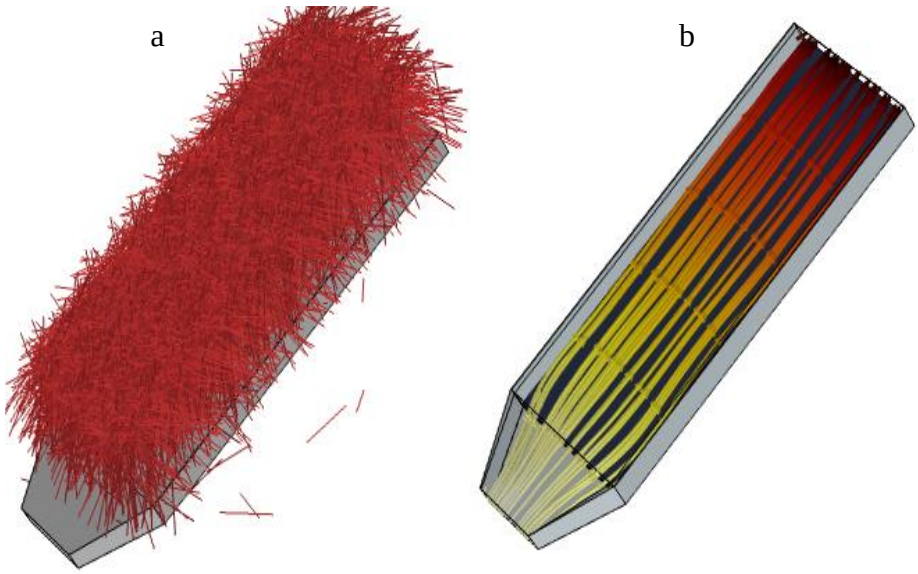

Fig. ٥ An example of the ray paths and heat flux on the solar air heater

٥,٢. Analyzing Thermal Data

Several distances between the absorber and base of the collector in the same conditions are chosen for the model simulation to compare the outcomes of the SAHs with various absorb position distances. In particular, the normalized ambient temperature and solar irradiation values for a typical workday in Jul in Yasouj (a city in southwest Iran with latitudes of 30.6684 N and 51.5875 E, respectively, are chosen for this purpose. Irradiation from the sun and ambient temperature are shown in **Fig. 6**. In the simulations, inlet mass flow rates and ambient wind velocity are taken as 0.02 m/s and 0.08 kg/s, respectively.

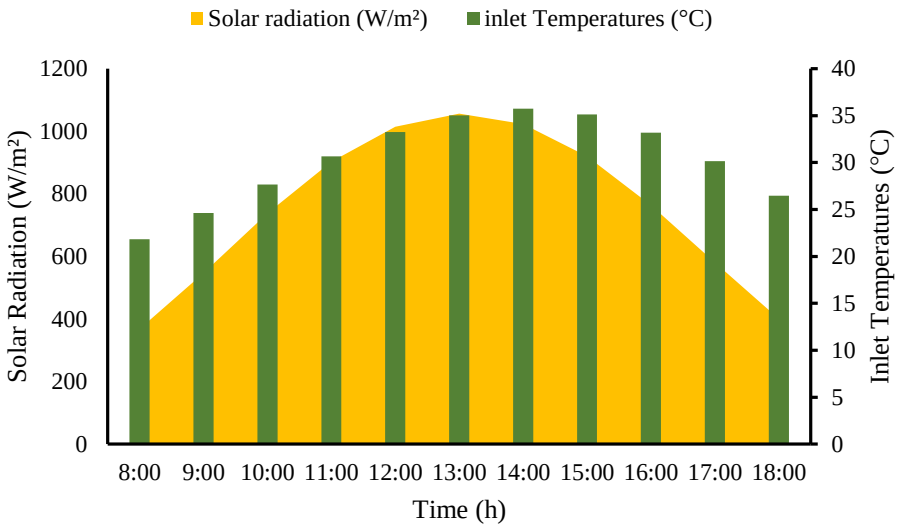

Fig. ٦ On a typical day in July, in Yasouj, Iran, ambient air temperature and solar irradiation [٤١].

٥,٣. Results

The use of plate Type V is the measure to enhance the heat transfer by providing more heat transfer area to air in the same length of the absorber plate compared to plate Type I, Type II, Type III, and Type IV. when the user Type V more heat is received because the amount of air that flow over the absorber also flows under the absorber, which provides more heat, and reduce heat losses. The temperature of the outlet air of the system for different locations of the absorber plates at 0.02 kg/s mass flow rate are shown in **Fig. 7.** A range of maximum temperatures was measured for Tout Type I, Tout Type II, Tout Type III, Tout Type IV, and Tout Type V, which are 75.37, 73.98, 77.87, 82,9, and 83 °C, respectively. During the late afternoon, solar radiation increases, and the heaters' temperatures increase to their maximum value at 14:00. Consequently, the plate surface heaters Type V have higher outlet temperatures than other Types of flat plate heaters. Computational fluid dynamics (CFD) and heat transfer tools have been used to investigate solar air heaters, revealing their physics and rendering them a powerful tool for optimizing flow parameters and geometrical parameters.

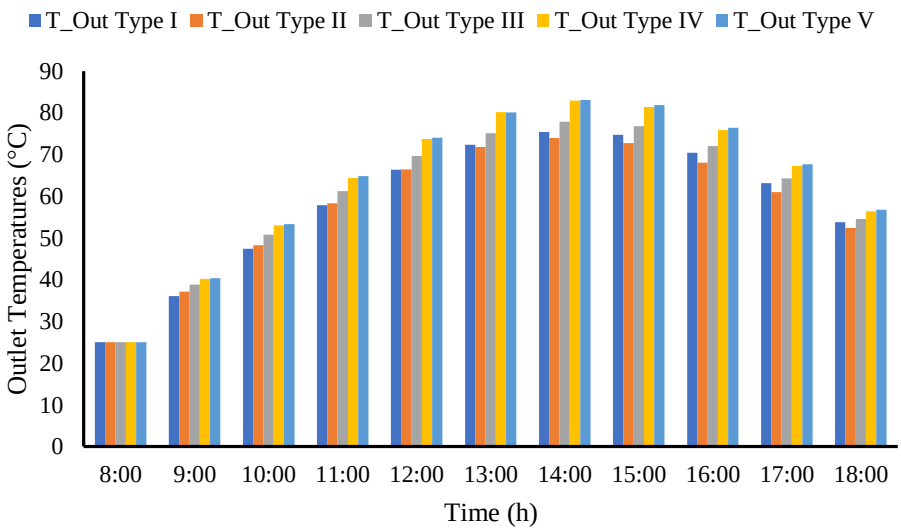

Fig. ٧ The temperature of the air outlet at different distances a flat absorber from the collector base.

Temperature efficiency with various absorber locations from bottom of collector. There is a decrease in values during the middle of the day compared to the morning and evening. Due to the higher temperature of the system's primary components at midday, there are more thermal losses at that time. Also, the thermal efficiencies of the systems are higher at the end of the day than at the beginning of the day. Earlier conditions impact the system's immediate performance while it operates under changing operational settings. In such solar systems, a portion of the absorbed solar heating capacity is absorbed in different faces of the system as sensible heat. This is done as air passes through the SAHs and is in heat contact with adjacent components. When the solar irradiation decreases, the absorber absorbs less heat, decreasing air temperature. This results in sensible heat being transferred in the opposite direction from the collector's components to the air, leading to higher thermal efficiency; based on **Fig. 8**. SAH, the absorber location at the bottom of the collector is 0.8 cm and has the highest average daily thermal efficiency. The system's thermal efficiency is significantly affected by the different locations of the absorber plates. At a mass flow of 0.02 kg/s, Type I, Type II, Type III, Type IV, and Type V of SAH are compared for their instantaneous thermal efficiency. Solar radiation is measured at 368-1056.4 W/m2, and the maximum values are 76.5, 72.35, 78.3, 83.77, and 84.75%, respectively. With the

location of the absorber plate, the surface area can be increased, leading to faster convection heat transfer. The air heater becomes more efficient as a result. Also, compared with the case without distance, heater efficiency increases by 8.2% when choosing a suitable location for absorber plates.

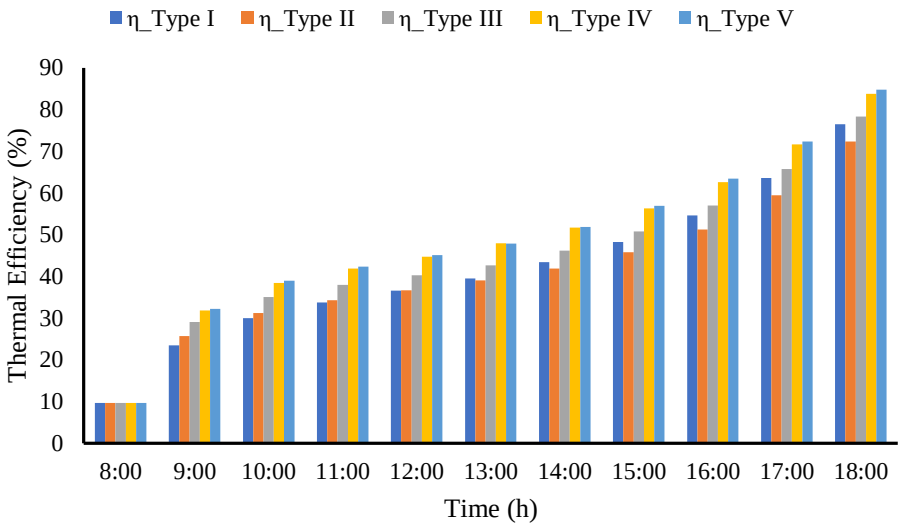

Fig. ٨ The variation of thermal efficiency.

Heat flows through the insulation of the collector mainly by conduction, which is the reason for energy loss through the bottom and edges. Absorbers' plate location affects local convective heat transfer coefficients when the airflow through the top and bottom absorbers surfaces is shown in **Fig. 9**. Heat transfer coefficients are higher with increased surface area. Compared with mornings and evenings, the values decrease during the middle of the day. At midday, there are more heat losses because the system's primary components are at a higher temperature. At the end of the day, the heat transfer coefficient is higher than at the beginning. The instantaneous heat transfer coefficient of Type I, Type II, Type III, Type IV, and Type V of SAH is compared at a mass flow rate of 0.02 kg/s. According to the measurements, solar radiation ranges from 368 to 1056.4 W/m^2, with maximum values of 9.67, 7.7, 9.41, 14.56, and 17 (W/m^2. K).

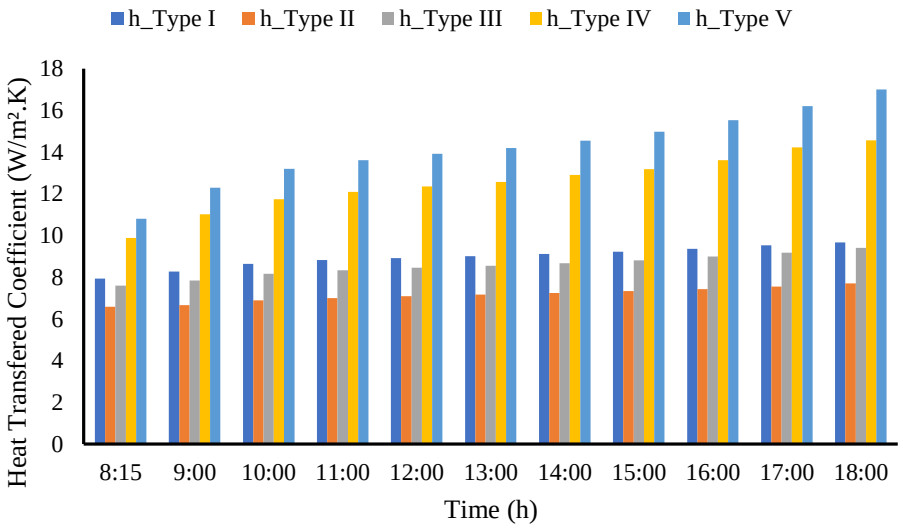

Fig. ٩ Heat transfer coefficients with various locations of absorber plates

Nusselt number distributions strongly depend on the absorbing plates' geometry and location. The optimal configuration allows the airflow to follow the absorbing surfaces' trajectory and contact them on both sides. There are five absorber plate locations among the absorber Types shown in **Fig. 10**. Due to the increasing amount of area and air over the top and bottom, surface heat is removed from the heated absorber plate and transferred to the fluid. In comparison to mornings and evenings, midday values decrease. Due to the higher temperature of the system's primary components at midday, there is more heat loss. The Nusselt number is greater at the end of a day than at the beginning. At a mass flow rate of 0.02 kg/s, the instantaneous Nusselt number of Type I, Type II, Type III, Type IV, and type V of SAH are compared. There are maximum values of 6.7, 3.3, 5.44, 15.64, and 21.1 for solar radiation, based on measurements.

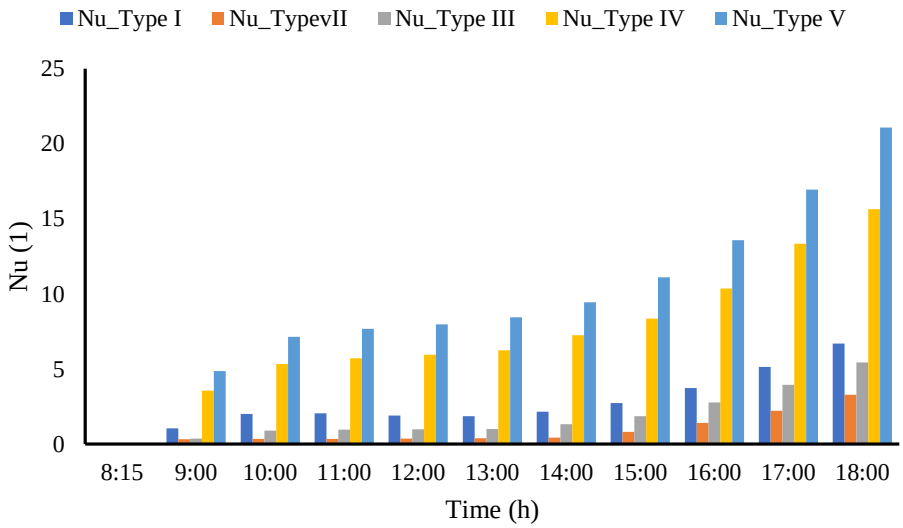

Fig. ١٠ Nusselt Number predictions for various absorber plate locations.

affect the system's thermal efficiency and, air outlet temperature. This is shown in **Fig. 11**. The temperatures at the outlet should determine the type of inlet air flow rate to use. When air is introduced at a higher rate, it reduces the average temperature of all the system, and as a consequence, the overall performance is improved. Due to reduced heat losses, the system achieves higher thermal efficiency. The system's thermal efficiency can be near 100% in some cases during evening hours. Therefore, this variation from the steady state represents the heat absorbed by the system components as a portion of thermal energy. At a mass flow rate of 0.02, 0.04, 0.06, and 0.08 kg/s, the instantaneous outlet temperatures with thermal efficiency of Type V of SAH. There are maximum values of 82, 67, 58, and 53 ^{o}C with 84.75, 93, 96.6, and 99.1%.

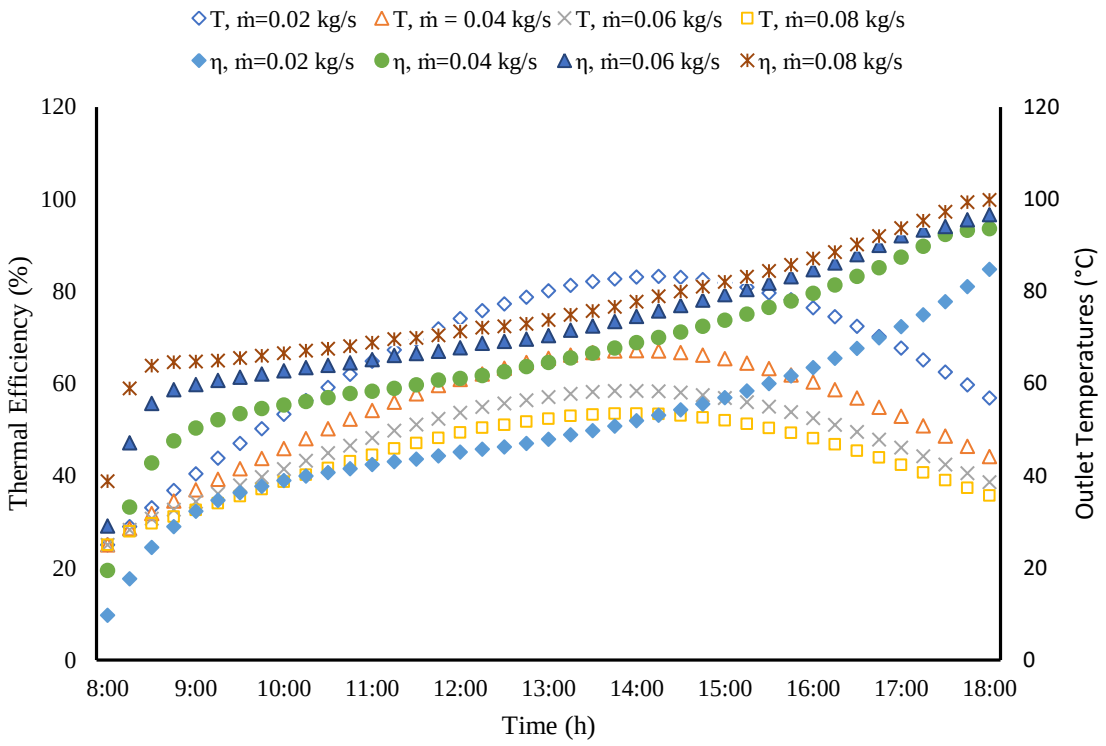

Fig. ١١ The air outlet temperature and thermal efficiency of the SAHs for different air inlet rates with absorber plate location Type V.

٦. Conclusion

This paper investigated the use of an array of SAHs as a new type of solar air heater. The system's simultaneous optical and thermal analysis was conducted using coupled ray tracing and FEM simulation techniques. In the presence of non-uniform heat flux on the absorber plate surfaces, the system's thermal performance was analyzed under different operational conditions. A 3D CFD simulation was created in the form of a model for the entire system as well as the temperature and flow rate of inlet air affected the temperature of hot air produced. There was an analysis of the thermal efficiency, heat transfer coefficient, and Nusselt number of the absorber plate at various locations in the SAHs. Due to variation in heat flux distribution, the location of the absorber plate in the collectors significantly impacts the system efficiency. In order to achieve the highest thermal efficiency of the system, a d of 0.008 m was determined as the most appropriate location for the absorber plate. Under specified operating conditions, system

efficiency averages around 84.75%, while less than 76.5% for absorbing plates near the bottom of the collector.

References

[1] Singh Bisht V, Kumar Patil A, Gupta A. Review and performance evaluation of roughened solar air heaters. Renewable and Sustainable Energy Reviews 2018;81. https://doi.org/10.1016/j.rser.2017.08.036.

[2] Singh I, Singh S. A review of artificial roughness geometries employed in solar air heaters. Renewable and Sustainable Energy Reviews 2018;92. https://doi.org/10.1016/j.rser.2018.04.108.

[3] Arunkumar HS, Vasudeva Karanth K, Kumar S. Review on the design modifications of a solar air heater for improvement in the thermal performance. Sustainable Energy Technologies and Assessments 2020;39. https://doi.org/10.1016/j.seta.2020.100685.

[4] Abuşka M. Energy and exergy analysis of solar air heater having new design absorber plate with conical surface. Applied Thermal Engineering 2018;131. https://doi.org/10.1016/j.applthermaleng.2017.11.129.

[5] Gürel AE, Yıldız G, Ergün A, Ceylan İ. Exergetic, economic and environmental analysis of temperature controlled solar air heater system. Cleaner Engineering and Technology 2022;6. https://doi.org/10.1016/j.clet.2021.100369.

[6] Jain SK, Agrawal G das, Misra R. Heat transfer augmentation using multiple gaps in arc-shaped ribs roughened solar air heater: an experimental study. Energy Sources, Part A: Recovery, Utilization and Environmental Effects 2021;43. https://doi.org/10.1080/15567036.2019.1607945.

[7] kumar R, Kumar R, Kumar S, Thapa S, Sethi M, Fekete G, et al. Impact of artificial roughness variation on heat transfer and friction characteristics of solar air heating system. Alexandria Engineering Journal 2022;61. https://doi.org/10.1016/j.aej.2021.06.031.

[8] Sajawal M, Rehman TU, Ali HM, Sajjad U, Raza A, Bhatti MS. Experimental thermal performance analysis of finned tube-phase change material based double pass solar air heater. Case Studies in Thermal Engineering 2019;15. https://doi.org/10.1016/j.csite.2019.100543.

[9] Abdullah AS, Amro MI, Younes MM, Omara ZM, Kabeel AE, Essa FA. Experimental investigation of single pass solar air heater with reflectors and turbulators. Alexandria Engineering Journal 2020;59. https://doi.org/10.1016/j.aej.2020.02.004.

[10] Korpale VS, Deshmukh SP, Mathpati CS, Dalvi VH. Numerical simulations and optimization of solar air heaters. Applied Thermal Engineering 2020;180. https://doi.org/10.1016/j.applthermaleng.2020.115744.

[11] Khatri R, Goswami S, Anas M, Sharma S, Agarwal S, Aggarwal S. Performance evaluation of an arched plate solar air heater with porous aluminum wire mesh cylindrical fins. Energy Reports 2020;6. https://doi.org/10.1016/j.egyr.2020.11.177.

[12] Zhu T, Zhang J. A numerical study on performance optimization of a micro-heat pipe arrays-based solar air heater. Energy 2021;215. https://doi.org/10.1016/j.energy.2020.119047.

[13] Gilago MC, Chandramohan VP. Performance evaluation of natural and forced convection indirect type solar dryers during drying ivy gourd: An experimental study. Renewable Energy 2022;182:934–45. https://doi.org/10.1016/j.renene.2021.11.038.

[14] Lingayat AB, Chandramohan VP, Raju VRK, Meda V. A review on indirect type solar dryers for agricultural crops – Dryer setup, its performance, energy storage and important highlights. Applied Energy 2020;258. https://doi.org/10.1016/j.apenergy.2019.114005.

[15] Goud M, Reddy MVV, V.P. C, S. S. A novel indirect solar dryer with inlet fans powered by solar PV panels: Drying kinetics of Capsicum Annum and Abelmoschus esculentus with dryer performance. Solar Energy 2019;194:871–85. https://doi.org/10.1016/J.SOLENER.2019.11.031.

[16] Fudholi A, Sopian K, Ruslan MH, Alghoul MA, Sulaiman MY. Review of solar dryers for agricultural and marine products. Renewable and Sustainable Energy Reviews 2010;14:1–30. https://doi.org/10.1016/j.rser.2009.07.032.

[17] Madhlopa A, Jones SA, Kalenga Saka JD. A solar air heater with composite-absorber systems for food dehydration. Renewable Energy 2002;27. https://doi.org/10.1016/S0960-1481(01)00174-4.

[18] Sulaiman SA, Taha FFF. Drying of Oil Palm Fronds Using Concentrated Solar Thermal Power. Applied Mechanics and Materials 2014;699. https://doi.org/10.4028/www.scientific.net/amm.699.449.

[19] Boukelia TE, Mecibah MS. Parabolic trough solar thermal power plant: Potential, and projects development in Algeria. Renewable and Sustainable Energy Reviews 2013;21:288–97. https://doi.org/10.1016/J.RSER.2012.11.074.

[20] Soria R, Lucena AFP, Tomaschek J, Fichter T, Haasz T, Szklo A, et al. Modelling concentrated solar power (CSP) in the Brazilian energy system: A soft-linked model coupling approach. Energy 2016;116. https://doi.org/10.1016/j.energy.2016.09.080.

[21] Ceylan I, Gürel AE, Ergün A, Tabak A. Performance analysis of a concentrated photovoltaic and thermal system. Solar Energy 2016;129. https://doi.org/10.1016/j.solener.2016.02.010.

[22] Kasaeian A, Sharifi S, Yan WM. Novel achievements in the development of solar ponds: A review. Solar Energy 2018;174:189–206. https://doi.org/10.1016/J.SOLENER.2018.09.010.

[23] Tabor H. Solar ponds. Solar Energy 1981;27:181–94. https://doi.org/10.1016/0038-092X(81)90120-1.

[24] Madadi Avargani V, Divband M. Performance evaluation of a solar water heating system with glass-covered parabolic trough concentrators, under different system tracking modes. Journal of Thermal Analysis and Calorimetry 2022;147:4873–88. https://doi.org/10.1007/s10973-021-10845-9.

[25] Kannan N, Vakeesan D. Solar energy for future world: - A review. Renewable and Sustainable Energy Reviews 2016;62:1092–105. https://doi.org/10.1016/j.rser.2016.05.022.

[26] Ravi Kumar K, Krishna Chaitanya NVV, Sendhil Kumar N. Solar thermal energy technologies and its applications for process heating and power generation – A review. Journal of Cleaner Production 2021;282:125296. https://doi.org/10.1016/j.jclepro.2020.125296.

[27] Trefilov VI, Schur D v., Pishuk VK, Zaginaichenko SY, Choba A v., Nagornaya NR. The solar furnaces for scientific and technological investigation. Renewable Energy 1999;16:757–60. https://doi.org/10.1016/S0960-1481(98)00273-0.

[28] Madadi Avargani V, Norton B, Rahimi A, Karimi H. Integrating paraffin phase change material in the storage tank of a solar water heater to maintain a consistent hot water output temperature. Sustainable Energy Technologies and Assessments 2021;47:101350. https://doi.org/10.1016/j.seta.2021.101350.

[29] Kumar A, Layek A. Evaluation of the performance analysis of an improved solar air heater with Winglet shaped ribs. Experimental Heat Transfer 2022;35. https://doi.org/10.1080/08916152.2020.1838670.

[30] Aboghrara AM, Baharudin BTHT, Alghoul MA, Adam NM, Hairuddin AA, Hasan HA. Performance analysis of solar air heater with jet impingement on corrugated absorber plate. Case Studies in Thermal Engineering 2017;10:111–20. https://doi.org/10.1016/j.csite.2017.04.002.

[31] Luan NT, Phu NM. Thermohydraulic correlations and exergy analysis of a solar air heater duct with inclined baffles. Case Studies in Thermal Engineering 2020;21. https://doi.org/10.1016/j.csite.2020.100672.

[32] Singh AK, Agarwal N, Saxena A. Effect of extended geometry filled with and without phase change material on the thermal performance of solar air heater. Journal of Energy Storage 2021;39. https://doi.org/10.1016/j.est.2021.102627.

[33] Azad R, Bhuvad S, Lanjewar A. Study of solar air heater with discrete arc ribs geometry: Experimental and numerical approach. International Journal of Thermal Sciences 2021;167. https://doi.org/10.1016/j.ijthermalsci.2021.107013.

[34] Saravanan A, Murugan M, Reddy MS, Ranjit PS, Elumalai P v., Kumar P, et al. Thermo-hydraulic performance of a solar air heater with staggered C-shape finned absorber plate. International Journal of Thermal Sciences 2021;168. https://doi.org/10.1016/j.ijthermalsci.2021.107068.

[35] Khanlari A, Sözen A, Şirin C, Tuncer AD, Gungor A. Performance enhancement of a greenhouse dryer: Analysis of a cost-effective alternative solar air heater. Journal of Cleaner Production 2020;251. https://doi.org/10.1016/j.jclepro.2019.119672.

[36] Abo-Elfadl S, Yousef MS, Hassan H. Energy, exergy, and enviroeconomic assessment of double and single pass solar air heaters having a new design absorber. Process Safety and Environmental Protection 2021;149. https://doi.org/10.1016/j.psep.2020.11.020.

[37] Singh S. Experimental and numerical investigations of a single and double pass porous serpentine wavy wiremesh packed bed solar air heater. Renewable Energy 2020;145. https://doi.org/10.1016/j.renene.2019.06.137.

[38] Bensaci CE, Moummi A, Sanchez de la Flor FJ, Rodriguez Jara EA, Rincon-Casado A, Ruiz-Pardo A. Numerical and experimental study of the heat transfer and hydraulic performance of solar air heaters with different baffle positions. Renewable Energy 2020;155. https://doi.org/10.1016/j.renene.2020.04.017.

[39] Farhan AA, Issam M.Ali A, Ahmed HE. Energetic and exergetic efficiency analysis of a v-corrugated solar air heater integrated with twisted tape inserts. Renewable Energy 2021;169. https://doi.org/10.1016/j.renene.2021.01.109.

[40] Esen H, Ozgen F, Esen M, Sengur A. Artificial neural network and wavelet neural network approaches for modelling of a solar air heater. Expert Systems with Applications 2009;36:11240–8. https://doi.org/10.1016/J.ESWA.2009.02.073.

[41] Madadi Avargani V, Zendehboudi S, Rahimi A, Soltani S. Comprehensive energy, exergy, enviro-exergy, and thermo-hydraulic performance assessment of a flat plate solar air heater with different obstacles. Applied Thermal Engineering 2022; 203:117907. https://doi.org/10.1016/J.APPLTHERMALENG.2021.117907.